

Cite this: *Phys. Chem. Chem. Phys.*, 2011, **13**, 13395–13402

www.rsc.org/pccp

PAPER

# Flow conditions in the vicinity of microstructured interfaces studied by holography and implications for the assembly of artificial actin networks

Sebastian Weiße,<sup>\*a</sup> Matthias Heydt,<sup>a</sup> Timo Maier,<sup>b</sup> Simon Schulz,<sup>b</sup>  
Joachim P. Spatz,<sup>bc</sup> Michael Grunze,<sup>ad</sup> Tamás Haraszti<sup>bc</sup> and Axel Rosenhahn<sup>ad</sup>

Received 18th January 2011, Accepted 3rd June 2011

DOI: 10.1039/c1cp20153k

Microstructured fluidic devices have successfully been used for the assembly of free standing actin networks as mechanical model systems on the top of micropillars. The assembly occurs spontaneously at the pillar heads when preformed filaments are injected into the channel. In order to reveal the driving mechanism of this localization, we studied the properties of the flow profile by holographic tracking. Despite the strong optical disturbances originating from the pillar field, 2  $\mu\text{m}$  particles were traced with digital in-line holographic microscopy (DIHM). Trajectories in the pillar free region and local alterations of the flow profile induced by the channel structure in the pillar decorated region can be distinguished. Velocity histograms at different z-positions reveal that the laminar flow profile across the channel shows a difference between the minimum in the z-component of the velocity field and the maximum of the overall velocity. This minimum drag in vertical direction is present at the top of the pillars and explains why biopolymer networks readily assemble in this region instead of forming a homogeneous three-dimensional network in between the pillars. On the basis of the observations we propose a new mechanism for actin network formation on top of the microstructures.

## Introduction

Microfluidic devices are widely used tools for studying soft matter,<sup>1–3</sup> creating chemical gradients,<sup>4,5</sup> quantifying adhesion strength<sup>6</sup> or as vessels for chemical reactions.<sup>7,8</sup> Introducing structures to the channel walls allows to control the flow profiles or to induce mixing of components in the liquid phase.<sup>9</sup> An important recent application of structured microfluidic devices is to serve as support for two-dimensional biomimetic actin cortex models, to study the physical-chemical properties of an actin network. These networks are constructed on the top of micropillars and look similar to the actin cortex and stress fibers of cells morphologically, containing freely accessible, suspended actin filaments, and a controlled physical-chemical environment for experiments.<sup>10,11</sup> The micropillars are built into a closed microfluidic channel system, which minimizes the amount of reagents used and gives full access for high resolution fluorescence microscopy to visualize the actin.

The usage of such flow channels is of great practical advantage and their design has been optimized experimentally in recent years with respect to biocompatibility and suitability for assembly of artificial fiber networks. The successful assembly of the actin networks can be imaged by confocal fluorescence microscopy and a typical image is shown in Fig. 1. However, the three-dimensional structure of the microchannel also complicates the boundary condition for the flow making it difficult to theoretically access the exact flow profile which plays a pivotal role in the assembly of the artificial networks.

One would expect that in the simplest case actin filaments get deposited homogeneously on all surfaces, thus on the channel walls and in between the pillars, resulting in a homogenous 3D network interconnecting the pillars. Though indeed most actin is present at the top and bottom channel walls, in the pillar region a network is only formed on top of the pillar heads and not between the pillars. In this work we address the underlying driving force that leads to the assembly of a 2D network on top of the pillar heads rather than a 3D network.

Obviously, an understanding of the assembly process requires knowledge about the flow field during the network formation within the microfluidic channel. A range of techniques is available to measure flow fields in microfluidic devices and many of them have been summarized in reviews by Adrian,<sup>12</sup> Hinsch<sup>13</sup> and Bayraktar.<sup>14</sup> Microscale particle image velocimetry ( $\mu\text{PIV}$ ) is probably the most common technique in this field. In  $\mu\text{PIV}$  the motion of small tracer particles is imaged to

<sup>a</sup> Applied Physical Chemistry, University of Heidelberg,  
Im Neuenheimer Feld 253, 69120 Heidelberg, Germany.  
E-mail: weisse@uni-heidelberg.de; Fax: +49 6221 545060;  
Tel: +49 6221 545064

<sup>b</sup> Biophysical Chemistry, University of Heidelberg,  
Im Neuenheimer Feld 253, 69120 Heidelberg, Germany

<sup>c</sup> Max-Planck-Institute for Intelligent Systems, Heisenbergstraße 3,  
70569 Stuttgart, Germany

<sup>d</sup> Institute for Functional Interfaces, IFG, Karlsruhe Institute of  
Technology, PO Box 3640, 76021 Karlsruhe, Germany

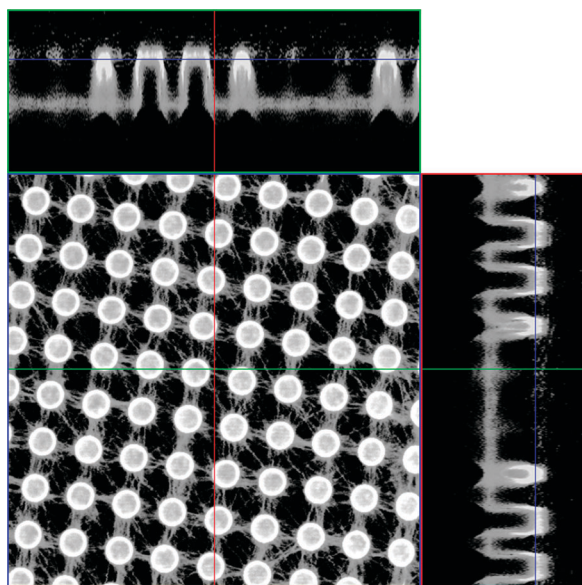


**Fig. 1** LSM image of an actin network on pillar fields. The image is enhanced using a polygonal look-up table to highlight the actin network. The cross-sectional cuts on the right side and on top show actin filaments being present at the root of the pillars and a thin network at the top. The thickness of the network on the top is estimated to be about  $3\ \mu\text{m} \pm 0.5\ \mu\text{m}$ . The high visibility of the pillars is due to the short actin fragments wrapping around them. The height of the pillars is  $15\ \mu\text{m}$ , the spacing is  $10\ \mu\text{m}$ .

determine flow profiles.<sup>15,16</sup> Most of these techniques detect the motion of tracer particles in a single focal plane of a microscope and the subsequent analysis of different planes results in a complete 3D image of the flow profile. However, such an analysis is restricted to stable flow profiles and it is difficult to access the depth component of the flow across the experimental volume. Holographic particle image velocimetry (HPIV) overcomes this limitation as it allows to record three-dimensional information of a flow.<sup>17,18</sup> In a range of reported setups imaging optics or objectives are used.<sup>19,20</sup> Such setups require careful calibration of the optics as the obtained holograms result as a combination of the natural propagation of the wavefront and the propagation of the light through the objective. Especially the limited focal depth of some imaging optics must be considered when designing such an experiment. Completely lensless setups circumvent such complications and a projection-based magnification allows capturing large volumes between a point source and the detector.<sup>21</sup>

Lensless in-line holographic microscopy as introduced by Gabor<sup>22</sup> records a diffraction pattern, the so-called hologram, generated by a sample illuminated with a coherent, divergent electromagnetic wave. For detection, one nowadays makes use of digital recording by CCD- or CMOS-modules. Since the phase information is encoded as a modulation of the amplitude, three-dimensional information about the probed volume is acquired as intensity information measured by the detector. In this work we apply point source laser in-line holographic microscopy as described earlier.<sup>23</sup> The acquired holograms can be reconstructed using the Kreuzer implementation of the Kirchhoff-Helmholtz reconstruction formula.<sup>23</sup> If one acquires a sequence of holograms of moving objects such as swimming

microorganisms<sup>24</sup> or tracer particles, a four-dimensional set of information is provided, consisting of three spatial coordinates and the temporal coordinate. Using the most recent progress in this field of research, this spatio-temporal information can be retrieved and analyzed from holographic movies by automated computer programs.<sup>25,26</sup>

Constant improvement of digital image acquisition systems<sup>27</sup> and the increasingly available computational power make such coherent imaging techniques more and more attractive for 3D tracking. Holographic microscopy has found numerous applications especially for tracking object positions of tracers in microfluidics<sup>19,23,28–30</sup> and swimming microorganisms in biology,<sup>24,31–36</sup> but also for phase sensitive imaging.<sup>37–43</sup> These examples show that holographic microscopy has emerged as a versatile tool for 4D tracking applications.

## Materials and methods

### Flow channels

Microfluidic channels were built using standard soft-lithography methods, as described elsewhere.<sup>44</sup> They consisted of two parts: a  $40\ \mu\text{m}$  high channel constructed in a thin layer of PDMS on a microscope cover slip as the bottom part. And a top part comprised of a PDMS block a few millimeters in height structured with a  $5 \times 5\ \text{mm}^2$  pillar field. The pillars were  $5\ \mu\text{m}$  in diameter and  $15\ \mu\text{m}$  in height, with  $20\ \mu\text{m}$  center-to-center spacing, totaling in about 62500 pillars.<sup>10</sup>

To visualize the liquid flow in the channel a 1 : 500 diluted stock suspension of  $2\ \mu\text{m}$  polystyrene beads (Polybead, Polysciences Europe, Germany) was pumped through the channel at a flow rate of  $5\ \mu\text{l}/\text{min}$  using a syringe pump (Harvard Apparatus Pico Plus syringe pump, Harvard Apparatus, USA). The flow rate was chosen to be suitable to acquire sufficiently long traces with the given camera frame rate and allow for stable flow conditions at the same time.

### Actin networks

Actin networks were prepared as described elsewhere.<sup>44</sup> Briefly, globular actin (G-actin) and *N*-ethylmaleimide modified heavy meromyosin (NEMHMM) were prepared from rabbit skeletal muscle as described by Pardee<sup>45</sup> and MacLean-Fletcher.<sup>46</sup> F-actin was polymerized from G-actin in a polymerization buffer (2.0 mM TRIS, 2 mM  $\text{MgCl}_2$ , 100 mM KCl, 0.2 mM  $\text{CaCl}_2$ , 0.2 mM DTT, 0.5 mM ATP, pH 7.4) for 20 min at room temperature or alternatively for 30 min on ice. The monomer concentration at the beginning of polymerization was  $5\ \mu\text{M}$ . After the given time, the actin molecules were labeled using phalloidin-TRITC (#P1951, Sigma-Aldrich Chemie GmbH, Germany) in an equimolar ratio to the G-actin. In order to form actin networks inside the flow cells, NEMHMM ( $5\ \mu\text{M}$  aqueous solution) was injected and incubated for 20 min. NEMHMM binds to the PDMS surface nonspecifically and is capable of binding actin, however its motor activity is blocked. The effects of proteins adsorbed to areas not of interest, such as the wall of the flow channel, were negligible on the network formation due to the relatively large dimensions of the experimental volume. After incubating in NEMHMM, the test buffer solution (25 mM imidazole,

1 mM EGTA, 4 mM  $\text{MgCl}_2$ , 25 mM KCl; pH = 7.4) was used to rinse the flow cell (about 50 microliters) and subsequently the labeled filamentous actin was injected. The test buffer was also used through fluorescence imaging experiments.

### Laser scanning confocal microscopy

Laser scanning confocal microscopy was performed using a Zeiss Axiovert 200 microscope with an LSM5 laser scanning module and the original Zeiss software. The objective used was a water immersion 40 $\times$  C-APOCHROMAT (NA = 1.2) from Zeiss. The pixel resolution was 0.22  $\mu\text{m}/\text{pixel}$  in xy-directions and 0.5  $\mu\text{m}/\text{pixel}$  in z-direction.

### Digital in-line holographic microscopy

The digital holographic microscope employed in this study follows directly the implementation described earlier by Kreuzer and coworkers.<sup>43</sup> All optical elements were set up in the in-line geometry. A diode-pumped solid-state-laser (IMM Meßtechnologie, Germany) working at a wavelength of 532 nm in continuous wave (CW)-mode with a power of 30 mW illuminated a pinhole with a diameter of 500 nm. To improve the photon flux through the pinhole, the laser beam was focused by a 20  $\times$  objective with NA = 0.4 (Euromex Microscopes, The Netherlands). A CCD-OEM module (Lumenera Corp., Canada) with 1392  $\times$  1040 pixels (1280  $\times$  1024 active pixels), detector size of 9.0  $\times$  6.7 mm<sup>2</sup> (8.3  $\times$  6.6 mm<sup>2</sup> active pixel area) and a frame rate of 15.4 Hz was used as detector and positioned at a distance of 14 mm behind the aperture with the sample between the two (compare schematic in Fig. 2). This results in a numerical aperture of NA = 0.23 for the given setup, where the numerical aperture is given by  $\text{NA} = D/(2L)$  with D being the detector's side length and L the camera-pinhole distance. The given setup provides a spatial resolution of 1.4  $\mu\text{m}$ .

### Data reconstruction and analysis

Data presented in this work are based on 1000 consecutively recorded holograms. Before the reconstruction step, holograms were cropped to their central 1024  $\times$  1024 pixels. Data reconstruction and coordinate determination for trajectory visualization were carried out according to previously published methods.<sup>23,31,32,47</sup> In brief, after subtraction of a source hologram single holograms were reconstructed in 1  $\mu\text{m}$  steps in the z-direction. A sufficiently small z-stepping is important to make the depth determination as accurate as possible. The holograms were reconstructed at distances between 570  $\mu\text{m}$  and 770  $\mu\text{m}$  from the pinhole, to image the channel region and its surroundings. Due to the divergence of the beam,<sup>21</sup> the field of view changes from 269  $\times$  269  $\mu\text{m}^2$  to 363  $\times$  363  $\mu\text{m}^2$  throughout the observation volume. As described previously by our group,<sup>32</sup> three different projections can be calculated from these volume reconstructions. Particle positions were extracted from these projections on a frame-by-frame basis by a computer-aided algorithm, which follows single particles and interrupts for user intervention in the case of position uncertainties, e.g. if particle trajectories are crossing.<sup>32</sup> In total, 543 tracer particle trajectories were extracted resulting in a total of 3757 data points.

### Results and discussion

In Fig. 3, a single hologram (a), a difference hologram consisting of 36 holograms representing the flow over approximately 3.5 s (b), and the reconstruction of the difference hologram (c) are shown. The difference hologram is generated by consecutively adding and subtracting holograms of a time series as described by the Kreuzer group.<sup>36</sup> As the result of this subtraction, the reconstruction contains only information of objects changing with time, i.e. in our case only information about the moving 2  $\mu\text{m}$  tracer particles. The trajectory of a

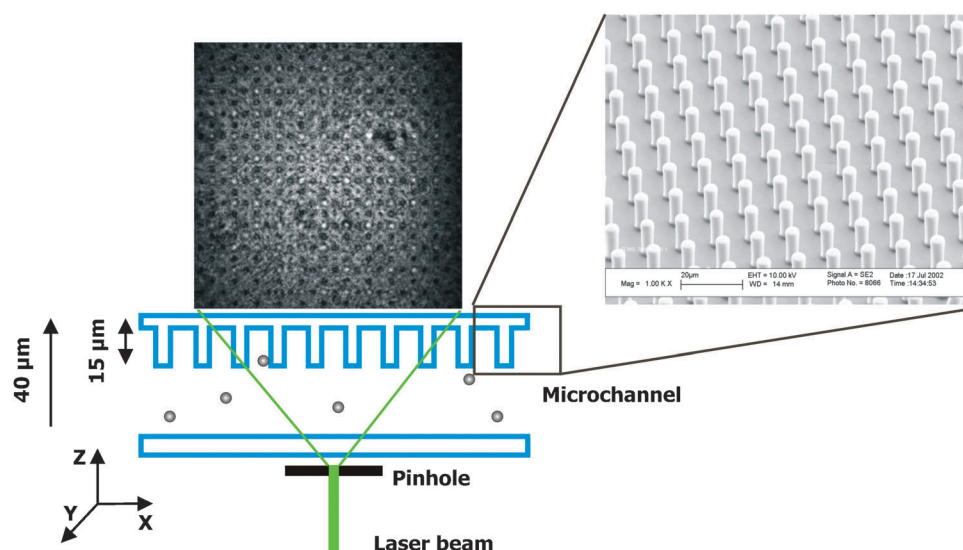


**Fig. 2** Schematic representation of the holographic microscopy experiment to characterize the flow properties in structured microchannels. The microfluidic device is illuminated with a divergent light cone produced by scattering laser light off a pinhole. The diffraction pattern is recorded with a CCD-chip. The inset shows a scanning electron microscopy picture of the pillar array with 1000 $\times$  magnification.



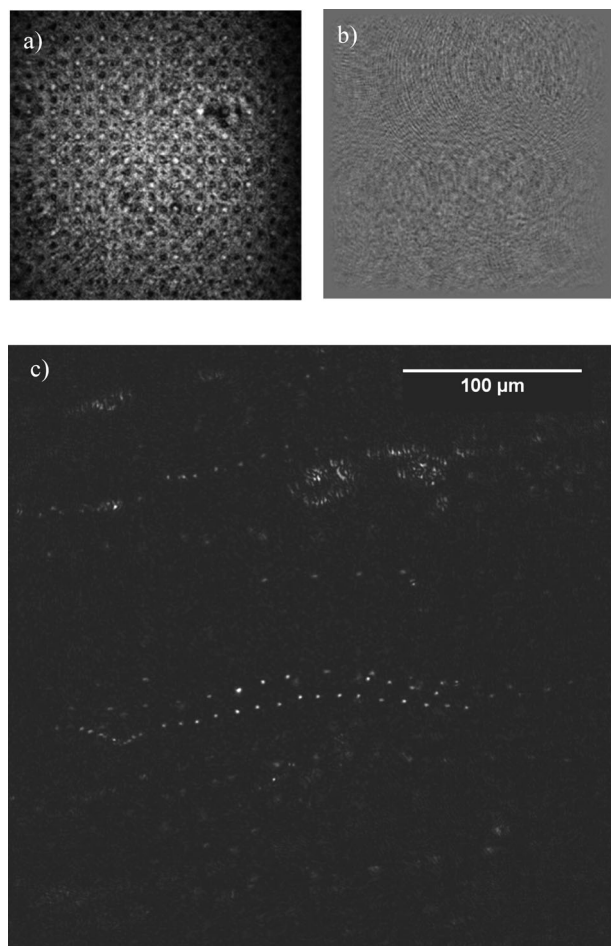


**Fig. 3** (a) Single hologram showing the diffraction pattern from the pillar field and some tracer particles, (b) difference hologram of a series of 36 individual holograms, and (c) reconstruction of (b) at a focal plane,  $z = 690 \mu\text{m}$  away from the pinhole.  $\text{NA} = 0.23$ .

tracer particle moving in the pillar region of the channel in Fig. 3c is of surprisingly good quality given the fact that the dominating diffraction pattern in the hologram (a) is caused by the pillar array. The reason why tracking is possible despite these huge alterations of the scattering background lies in a large degree of redundancy in the hologram of a point scatterer.<sup>36</sup> This becomes obvious when looking at the difference hologram in Fig. 3b showing that the scattering pattern of a single particle, and thus its position information, is encoded across a relatively large area, typically about  $100 \times 100$  pixels for the given experiment. Even though the pillar field may alter the intensity at some points, the correct position can still be restored. To demonstrate the robustness of the method, we compare the measured intensities of a single hologram, a difference hologram, and a reconstruction. The calculation was carried out by comparing line profiles of areas containing tracer particles with such not containing tracer information in the respective images (Fig. 4). The results support the visual impression that the pattern originating from the pillar field dominates the hologram. The intensity of the fringes caused by the tracer particles is about 50% of the scattering intensity caused by the microstructured array. Nevertheless the signal-to-noise

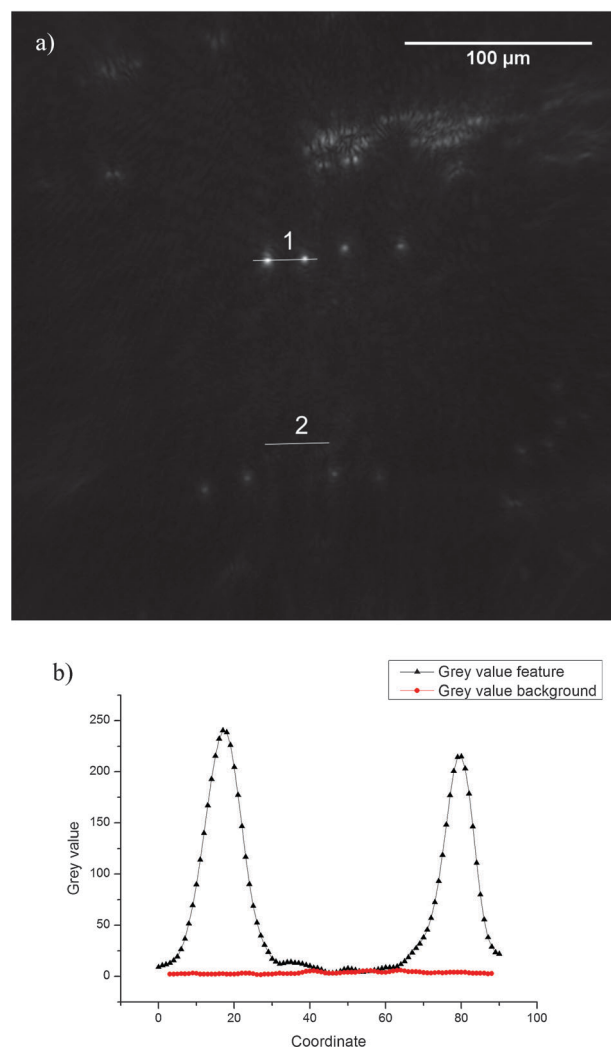


**Fig. 4** Line profiles to determine the signal-to-noise-ratio in a reconstructed image. (a)  $xy$ -Reconstruction with line profiles; 1 indicates the line profile for the object information and 2 for the background. (b) Line profiles for objects (black triangles) and the background (red circles).

ratio (SNR) of the reconstructions of difference holograms is as high as  $\text{SNR} = 53$ . For the used holographic setup the typical error of the position determination is  $500 \text{ nm}$  in the  $xy$ -projection and  $2.5 \mu\text{m}$  in the  $z$ -projection, which is in agreement with earlier studies carried out with a similar setup<sup>32</sup> and motile algal spores with a diameter of  $5 \mu\text{m}$ . The analyzed trajectories are depicted in Fig. 5. The  $xz$ -projection in Fig. 5b clearly indicates that the measured particle positions distribute across the whole channel height of  $40 \mu\text{m}$ .

Based on the channel design one can expect different flow profiles in the vicinity of the top and the bottom channel walls: a smooth linear flow profile is expected along the main flat channel wall in the bottom region, and a more complex flow field between and around the pillar field close the top wall. Looking at individual traces (Fig. 6) these two regions in the channel can be well distinguished. Note that in Fig. 6 the data points within a trajectory can be conceived as equally spaced in time, therefore their spacing is a direct measure of the

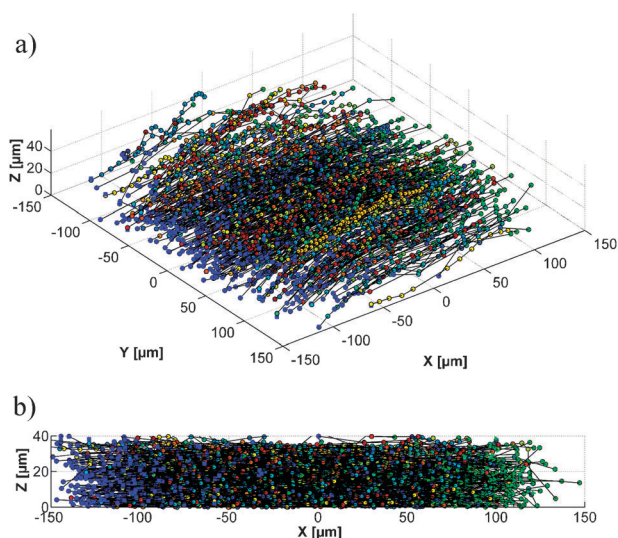


**Fig. 5** (a) 3D view of all 543 analyzed trajectories with a total of 3757 data points. Starting points of individual traces are marked by green triangles, end points by blue squares, (b) xz-projection of the particle trajectories.

particle velocity. In the free channel region, *i.e.* the lower 25  $\mu\text{m}$  of the channel (see also Fig. 2), trajectories are linear as expected for a laminar flow profile between parallel walls (Fig. 6a,b). In the topmost 15  $\mu\text{m}$  of the device, the pillar region, the velocity is decreased and the linearity of the trajectories is lost, thus the flow follows a more complex path through the pillar array (Fig. 6c–e). Interestingly, the xz-projection of the trajectories (Fig. 6e) clearly indicates the movement of the tracer particles along the z-axis, perpendicular to the flow (up to 20  $\mu\text{m}$  in some cases), which resulted in an in and out of focus behavior observed by classical video microscopy (data not shown). Occasionally interactions of the beads with the PDMS pillars were visible as the beads temporarily or permanently attached to the pillars.

To quantitatively characterize the flow conditions, velocity histograms were generated for different z-planes of the channel (“vz-histogram”). Velocities were binned in 100  $\mu\text{m}/\text{s}$  steps, heights in 5  $\mu\text{m}$  steps. In Fig. 7 these histograms were plotted against the z-coordinate to visualize the flow profile across the device. To take the different numbers of particles in each z-range into account, the histograms were normalized to the highest count rate in each z-slice. The normalized occurrence of velocities is color-coded according to the given grayscale. From Fig. 7 one can see that the maxima in the velocity distributions show, as expected, a parabola like flow profile in the vz-plane. It is noticeable that compared to the lower region of the channel, the velocity values for the upper part (25–40  $\mu\text{m}$  distance range), *i.e.* the pillar region, are significantly lower. Thus the pillars cause a deceleration of the liquid flow and as consequence an asymmetric flow profile can be observed.

Using the knowledge on flow velocity between the pillars with a flow speed  $v$  up to  $\sim 500 \mu\text{m}/\text{s}$  (compare Fig. 7) we can address the question if the particle behavior is caused by vortices. The Reynolds number  $\text{Re} = vd/\nu$  ( $d$  the size of the pillars of  $\sim 5\text{--}15 \mu\text{m}$  and  $\nu$  the kinematic viscosity of water ( $10^{-6} \text{ m}^2/\text{s}$ )) is  $\text{Re} \sim 10^{-2}$ . This means that vortices are rather

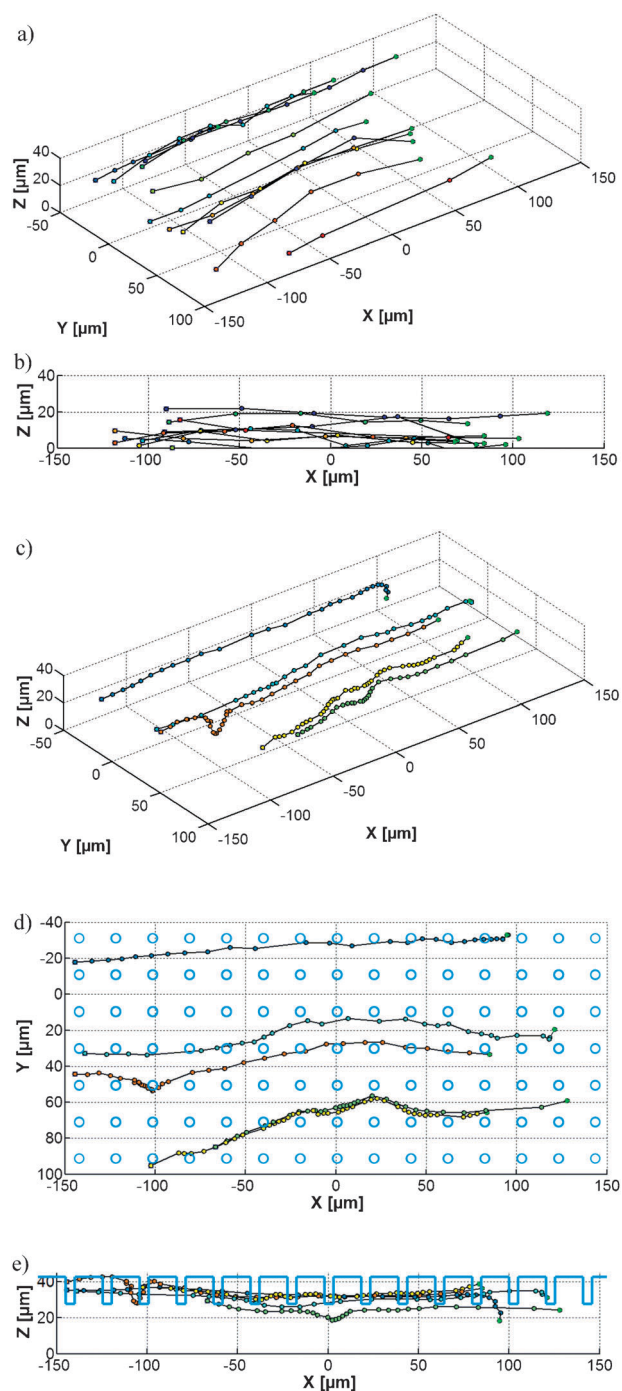


**Fig. 6** Typical trajectories for the pillar free channel region (a and b) and the structured channel region (c, d and e). (a) 3D view of some selected bead trajectories from the unstructured channel region ( $z = 0\text{--}25 \mu\text{m}$ ), (b) view of the same trajectories as in (a) but viewed as the channel cross section (xz-projection) in the flow direction, (c) selected trajectories in the pillar region. (d) Trajectories in (c) viewed as channel top view (xy-projection) with pillar positions indicated in blue. (e) Trajectories in (c) viewed as channel cross section (xz-projection) with pillar positions indicated in blue. Characteristic features are reduced velocity of the tracer particles in the pillar region (note the smaller point to point distances which correspond to a reduced velocity) as well as the circumvention of pillars, visible as turns in the trajectories.

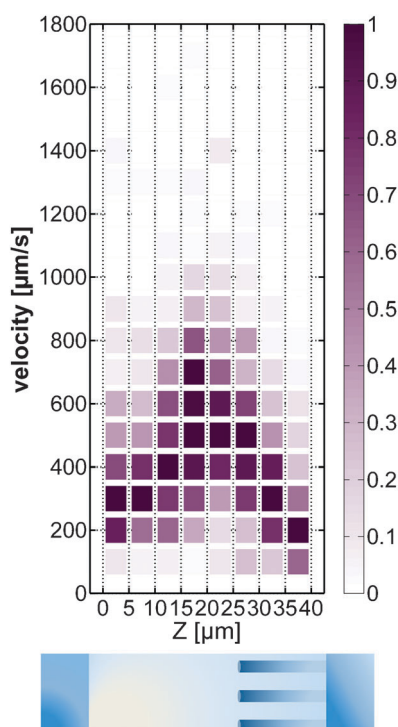


**Fig. 7** Flow profile of the microfluidic device given as velocity histograms with 5  $\mu\text{m}$  z-plane stepping across the channel and 100  $\mu\text{m/s}$  velocity binning. The normalized count rate is gray shaded according to the probability for a certain velocity to occur (colorbar). A schematic cross section of the channel is given in the lower part of the figure for easier perception of free channel and pillar decorated regimes.

unlikely as they are expected to occur at much larger Reynolds numbers, as it is found *i.e.* in the case of microfluidic mixers.<sup>19</sup>

It can be seen in Fig. 7 that not only the most likely velocity changes, but also the width of the velocity distribution. Full width at half maximum (FWHM) and most probable velocity values were interpolated from fitting a Gaussian based distribution to the velocity distributions in Fig. 7 at a given z-range similar to the analysis done by Heydt *et al.*<sup>32</sup> The results are summarized in Fig. 8 which shows the progression of most probable velocities and FWHM-values. The maximum of the most probable velocities and FWHM-values is located near the middle of the channel, which would be as expected between two plane-parallel walls with no pillars present. The presence of the pillar field causes an asymmetry of the flow profile as in the pillar region one observes a reduction of the most probable velocities compared to the free channel. We also note a steeper decrease in velocity approaching the pillar decorated channel wall compared to the flat wall.

Additionally to the velocity and FWHM analysis, the mean of the z-velocity component is expected to provide some insight how the in and out of focus drift of particles, observed with classical video microscopy, is distributed (Fig. 8, plot with green triangles). The overall z-component is 1–2 orders of magnitude smaller than the velocity of the particles in flow direction (note different scales of the two y-axis in Fig. 8). In the region of the pillar heads, the z-component of the velocity shows a clear minimum, shifted with respect to the

maximum of the most probable velocities. This minimum in the z-component of the velocity gives rise to the interpretation that in the region around the pillar tops, a focusing of the flow occurs which allows to enrich transported material, such as the *N*-ethylmaleimide modified heavy meromyosin (NEMHMM) and the actin to be assembled into a network. Interestingly, the graph implies that despite the reduced velocity there is a trend that material is transported out of the pillar region towards the pillar heads. Also from the middle of the channel where the highest velocity is observed, a material transport seems to occur towards the pillars. The drag towards the maximal velocity region of flow channels has been investigated extensively in the past and one would expect the particles being dragged into the middle part of the channel, where the velocity reaches its maximum (Fig. 8). The presence of the “lift force” was described by Saffman as early as in 1965<sup>48</sup> as a force proportional to the velocity gradient and the speed difference between the probing particle and the flow. In our current application we can assume that the particles accelerate until they move with the same velocity as the flow (canceling this effect), the attractive interaction between the PDMS and the polystyrene beads near the wall of the channel may slow the particles down enough resulting a maximum of the Saffman force in the vicinity of the walls. Furthermore, large enough structures on one channel wall will produce a modulation in the flow velocity along the z-direction, as it has been shown for 1-dimensional groove structures.<sup>49</sup> The pillar field present in our flow channel is a structure with 37.5% relative height, and a modulation length in the order of 12–50% of the channel height. This seems to be large enough for a perturbation of the flow field in the z-direction, resulting the unusual but highly useful asymmetric profile of the z-components of the flow velocities.

We suggest that this focusing close to the pillar heads is important for the mechanism causing actin filaments to assemble preferentially on the pillar heads as a quasi two-dimensional network<sup>10</sup> instead of forming a homogeneous three-dimensional network in between the pillars. Interpreting our findings as a mechanism, the process of actin network formation is envisioned as follows: The NEMHMM molecules attach nonspecifically to the PDMS surfaces at the three stagnancy planes, *i.e.* the top and the bottom of the flow channel where stagnancy occurs due to the flow velocity approaching zero and the top of the pillar heads, where stagnancy occurs due to the hydrodynamic focusing observed in this study. When flowing in the prepolymerized actin filaments, they have the greatest chance of interaction with the surface at the same stagnancy planes. When one point of a filament attaches to a NEMHMM molecule, the drag of the fluid flow exerts a torque on the filament turning it towards the same plane where the first point was trapped. The result is a network partially oriented in the direction of the flow. Partially because the filament most frequently hits another anchoring point before it can completely turn into the direction of the flow. Taking into account the semiflexible nature of F-actin, the turning of actin can be further hindered if the surface contact occurs over a larger distance or at multiple contact points.



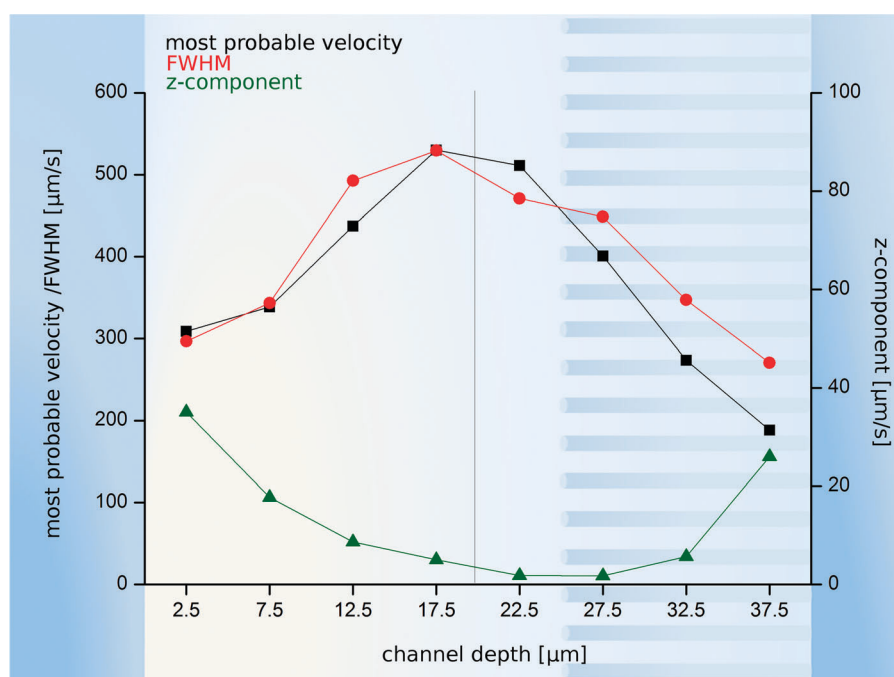


**Fig. 8** Comparison of the most probable velocity (black squares), full width at half maximum (red circles) (both left y-axis) and mean z-component of the velocity vectors (green triangles, right y-axis) across the channel height. The background illustrates to scale which is the free channel and which is the pillar region. The pillar region causes a deviation from the symmetric profile expected for the flow between two parallel plates. The gray line indicates the center of the channel. Note the different scales of the two y-axis for velocity and z-component.

## Conclusions

Characterizing the flow profile in microfluidic channels is important to optimize their performance and to quantitatively understand the hydrodynamic drag forces present. We have presented the application of digital in-line holographic microscopy to quantify the flow conditions in complexly structured microfluidic devices. The technique was found to be highly robust against optical disturbances arising from the pillar field. The reason for this high tolerance of holography can be seen in the large redundancy of information in holograms as the diffraction pattern extends over a large area. Trajectories of moving tracer particles were extracted from the reconstructed images and their quantitative analysis indicated different flow regimes in the device. Velocity histograms across the channel were used to identify the spatial distribution of flow velocity in planes at different depth. The flow within the pillar field was markedly different and it was possible to observe deviations from the ideal laminar flow expected between two smooth plates. The results show that the microstructures lead to a focusing flow effect close to the pillar heads in z-direction. The resulting stagnancy planes seem to play a key role in the successful assembly process of actin filaments between the tops of the pillar heads to form artificial actin networks. Based on these findings a mechanism for the 2D network formation is proposed.

## Acknowledgements

This work was supported by the “Graduiertenkolleg 1114-Optische Messtechniken für die Charakterisierung von Transportprozessen an Grenzflächen”, by the 6th framework

EU integrated project “AMBIO” and by the Office of Naval Research (grant N00014-08-1-1116). The authors also acknowledge the financial support of the Max-Planck-Society, the Volkswagen Foundation, the DFG Priority program 1164 “Nano- microfluidics” and the EU-FP6 STREP BIOMIMETICS program. Professor J. P. Spatz holds a Weston Visiting Professorship at the Weizmann Institute, Department of Molecular Cell Biology.

## References

- 1 E. Figallo, C. Cannizzaro, S. Gerecht, J. A. Burdick, R. Langer, N. Elvassore and G. Vunjak-Novakovic, *Lab Chip*, 2007, **7**, 710–719.
- 2 C. E. Sims and N. L. Allbritton, *Lab Chip*, 2007, **7**, 423–440.
- 3 R. Walder, A. J. Levine and M. Dennin, *Phys. Rev. E*, 2008, **77**, 011909.
- 4 S. K. W. Dertinger, D. T. Chiu, N. L. Jeon and G. M. Whitesides, *Anal. Chem.*, 2001, **73**, 1240–1246.
- 5 N. L. Jeon, S. K. W. Dertinger, D. T. Chiu, I. S. Choi, A. D. Stroock and G. M. Whitesides, *Langmuir*, 2000, **16**, 8311–8316.
- 6 C. Christophis, M. Grunze and A. Rosenhahn, *Phys. Chem. Chem. Phys.*, 2010, **12**, 4498–4504.
- 7 W. Ehrfeld and V. Hessel and H. Lowe in *Microreactors: New Technology for Modern Chemistry*, Wiley-VCH, Weinheim, 2000.
- 8 K. Geyer, J. D. C. Codee and P. H. Seeberger, *Chem.-Eur. J.*, 2006, **12**, 8434–8442.
- 9 A. D. Stroock, S. K. W. Dertinger, A. Ajdari, I. Mezic, H. A. Stone and G. M. Whitesides, *Science*, 2002, **295**, 647–651.
- 10 T. Haraszti, A. E. M. Clemen and J. P. Spatz, *ChemPhysChem*, 2009, **10**, 2777–2786.
- 11 W. H. Roos, A. Roth, J. Konle, H. Presting, E. Sackmann and J. P. Spatz, *ChemPhysChem*, 2003, **4**, 872–877.
- 12 R. J. Adrian, *Annu. Rev. Fluid Mech.*, 1991, **23**, 261–304.
- 13 K. D. Hinsch, *Meas. Sci. Technol.*, 1995, **6**, 742–753.

- 14 T. Bayraktar and S. B. Pidugu, *Int. J. Heat Mass Transfer*, 2006, **49**, 815–824.
- 15 R. Lindken, M. Rossi, S. Grosse and J. Westerweel, *Lab Chip*, 2009, **9**, 2551–2567.
- 16 J. G. Santiago, S. T. Wereley, C. D. Meinhart, D. J. Beebe and R. J. Adrian, *Exp. Fluids*, 1998, **25**, 316–319.
- 17 D. H. Barnhart, R. J. Adrian and G. C. Papen, *Appl. Opt.*, 1994, **33**, 7159–7170.
- 18 K. D. Hinsch, *Meas. Sci. Technol.*, 2002, **13**, R61–R72.
- 19 T. A. Ooms, R. Lindken and J. Westerweel, *Exp. Fluids*, 2009, **47**, 941–955.
- 20 S. Satake, T. Kunugi, K. Sato, T. Ito, H. Kanamori and J. Taniguchi, *Meas. Sci. Technol.*, 2006, **17**, 1647–1651.
- 21 H. J. Kreuzer, M. J. Jericho, I. A. Meinertzhagen and W. B. Xu, *J. Phys.: Condens. Matter*, 2001, **13**, 10729–10741.
- 22 D. Gabor, *Nature*, 1948, **161**, 777–778.
- 23 J. Garcia-Sucerquia, W. B. Xu, S. K. Jericho, P. Klages, M. H. Jericho and H. J. Kreuzer, *Appl. Opt.*, 2006, **45**, 836–850.
- 24 N. I. Lewis, W. B. Xu, S. K. Jericho, H. J. Kreuzer, M. H. Jericho and A. D. Cembella, *Phycologia*, 2006, **45**, 61–70.
- 25 L. Leal Taixe, M. Heydt, A. Rosenhahn and B. Rosenhahn, *IEEE Workshop on Motion and Video Computing (WMVC)*, Snowbird, Utah, USA, 2009.
- 26 L. Leal Taixe, M. Heydt, S. Weiße, A. Rosenhahn and B. Rosenhahn, *32nd Annual Symposium for Pattern Recognition (DAGM)*, Darmstadt, Germany, 2010, LNCS 6376, 283–292.
- 27 U. Schnars and W. Jüptner, *Appl. Opt.*, 1994, **33**, 179–181.
- 28 F. C. Cheong, B. Sun, R. Dreyfus, J. Amato-Grill, K. Xiao, L. Dixon and D. G. Grier, *Opt. Express*, 2009, **17**, 13071–13079.
- 29 J. Garcia-Sucerquia, W. Xu, S. K. Jericho, M. H. Jericho and H. J. Kreuzer, *Optik*, 2008, **119**, 419–423.
- 30 J. Sheng, E. Malkiel and J. Katz, *Exp. Fluids*, 2008, **45**, 1023–1035.
- 31 M. Heydt, A. Rosenhahn, M. Grunze, M. Pettitt, M. E. Callow and J. A. Callow, *J. Adhes.*, 2007, **83**, 417–430.
- 32 M. Heydt, P. Divos, M. Grunze and A. Rosenhahn, *Eur. Phys. J. E*, 2009, **30**, 141–148.
- 33 E. Malkiel, O. Alquaddoomi and J. Katz, *Meas. Sci. Technol.*, 1999, **10**, 1142–1152.
- 34 J. Sheng, E. Malkiel, J. Katz, J. Adolf, R. Belas and A. R. Place, *Proc. Natl. Acad. Sci. U. S. A.*, 2007, **104**, 17512–17517.
- 35 J. Sheng, E. Malkiel, J. Katz, J. E. Adolf and A. R. Place, *Proc. Natl. Acad. Sci. U. S. A.*, 2010, **107**, 2082–2087.
- 36 W. Xu, M. H. Jericho, H. J. Kreuzer and I. A. Meinertzhagen, *Opt. Lett.*, 2003, **28**, 164–166.
- 37 E. Cuhe, F. Bevilacqua and C. Depeursinge, *Opt. Lett.*, 1999, **24**, 291–293.
- 38 E. Cuhe, P. Marquet and C. Depeursinge, *Appl. Opt.*, 1999, **38**, 6994–7001.
- 39 T. Kreis, M. Adams and W. Jüptner, *Proc. SPIE-Int. Soc. Opt. Eng.*, 1997, **3098**, 224–233.
- 40 P. Marquet, B. Rappaz, P. J. Magistretti, E. Cuhe, Y. Emery, T. Colomb and C. Depeursinge, *Opt. Lett.*, 2005, **30**, 468–470.
- 41 H. Schmid, H. W. Fink and J. Kreuzer, *J. Vac. Sci. Technol., B*, 1995, **13**, 2428–2431.
- 42 U. Schnars and W. Jüptner, in *Digital Holography*, Springer, Berlin and Heidelberg, 2005.
- 43 W. B. Xu, M. H. Jericho, I. A. Meinertzhagen and H. J. Kreuzer, *Proc. Natl. Acad. Sci. U. S. A.*, 2001, **98**, 11301–11305.
- 44 T. Haraszti, S. Schulz, K. Uhrig, R. Kurre, W. Roos, C. H. J. Schmitz, J. E. Curtis, T. Maier, A. E. M. Clemen and J. P. Spatz, *Biophys. Rev. Lett.*, 2009, **4**, 17–32.
- 45 J. D. Pardee and J. A. Spudich, *Methods Enzymol.*, 1982, **85**, 164–181.
- 46 S. MacLean-Fletcher and T. D. Pollard, *Biochem. Biophys. Res. Commun.*, 1980, **96**, 18–27.
- 47 *US Pat.*, US 2004/0169903A1, 2004.
- 48 P. G. Saffman, *J. Fluid Mech.*, 1965, **22**, 385–400.
- 49 A. D. Stroock, S. K. Dertinger, G. M. Whitesides and A. Ajdari, *Anal. Chem.*, 2002, **74**, 5306–5312.